Editors' Suggestion | Featured in Physics

# Strong-Coupling Phases of Trions and Excitons in Electron-Hole Bilayers at Commensurate Densities

David D. Dai and Liang Fu
*Department of Physics, Massachusetts Institute of Technology, Cambridge, Massachusetts 02139, USA*

(Received 26 October 2023; accepted 28 March 2024; published 8 May 2024)

We introduce density imbalanced electron-hole bilayers at a commensurate 2:1 density ratio as a platform for realizing novel phases of electrons, excitons, and trions. Through the independently tunable carrier densities and interlayer spacing, competition between kinetic energy, intralayer repulsion, and interlayer attraction yields a rich phase diagram. By a combination of theoretical analysis and numerical calculation, we find a variety of strong-coupling phases in different parameter regions, including quantum crystals of electrons, excitons, and trions. We also propose an "electron-exciton supersolid" phase that features electron crystallization and exciton superfluidity simultaneously. The material realization and experimental signature of these phases are discussed in the context of semiconductor transition metal dichalcogenide bilayers.

DOI: 10.1103/PhysRevLett.132.196202

*Introduction.*—Recently, semiconductor transition metal dichalcogenide (TMD) heterostructures have emerged as an ideal platform for exploring quantum phases of matter. An extraordinarily rich variety of quantum states have been predicted and observed, including Mott-Hubbard and charge-transfer insulators [1–6], Wigner crystals [3,7–14], itinerant ferromagnets [15–20], interfacial ferroelectrics [21], heavy Fermi liquids [22–24], and spin-polaron liquids [16,25,26], as well as quantum spin Hall states [27,28] and quantum anomalous Hall states [29–38]. Remarkably, all these electronic phases realized in a single material system are rooted in one common ground—the two-dimensional electron (or hole) gas in monolayer TMDs. Here, the large effective mass and reduced screening favors strong interactions, and moiré bands in TMD heterostructures further enrich the physics, leading to much of the observed phenomena.

In addition to moiré physics, TMD heterostructures provide a material realization of electron-hole ($e$-$h$) bilayers featuring electrons and holes on spatially separated layers, whose densities can be independently tuned by top and bottom gate voltages [39]. The coexistence of positively and negatively charged particles supports both repulsion between like charges and attraction between opposite charges, enabling new phases of matter. When the densities of electrons and holes are equal, interlayer excitons with intrinsic out-of-plane dipole moments form, which may support high-temperature exciton superfluidity in an electrical insulator. Recently, thermodynamic evidence of excitonic insulator ground states has been observed in TMD bilayer $WSe_2/MoSe_2$ with $WSe_2$ as the hole layer and $MoSe_2$ as the electron layer separated by insulating $h$-BN layers that suppress recombination [40,41]. Moreover, density imbalanced electron-hole bilayers have attracted increasing interest owing to the interaction between charge carriers and dipolar excitons [42].

In this Letter, we study the strong-coupling phases of an imbalanced electron-hole bilayer at commensurate electron and hole densities $n_e/n_h = 2$, motivated by the following considerations. Because there is a net charge density $n = n_e - n_h \neq 0$, the Coulomb interaction between charged particles dominates in the low-density regime, favoring strong-coupling phases with crystalline order. This should be contrasted to the balanced electron-hole bilayer, where charge-neutral excitons condense into a superfluid at low densities because their mutual dipole-dipole interaction is parametrically weaker than the quantum kinetic energy. The particular choice of $n_e/n_h = 2$ is also motivated by the prospect of three-body bound states known as trions, which are charge-$e$ composite particles made of two electrons in the same layer bound to a hole in the other layer [43,44].

Through both theoretical analysis and numerical calculation, we find a number of ordered phases driven by strong interactions. These include bilayer electron-hole Wigner crystals, "composite crystals" of coexisting electrons and excitons, as well as exotic quantum phases without classical counterparts. In particular, we find a quantum supersolid made of electrons and excitons as well as a quantum crystal of trions in the low-density regime. Experimental signatures of these predicted phases in TMD bilayers are also discussed in the context of optical spectroscopy and transport measurements.

Before presenting our main results, we first consider the three-body problem of two electrons and one hole, which reside on spatially separated layers ($z = d$ and 0) and mutually interact through Coulomb forces. Classically, the minimum energy configuration is an electron and a dipole

 

that are far apart due to their residual repulsion. This dipole (equivalent to a classical exciton) consists of an electron and a hole sitting directly on top of each other, separated only by the layer distance $d$. For comparison, consider a "trion" charge cluster with the two electrons at $(\pm\mathbf{r}, d)$ and the hole at $(\mathbf{0}, 0)$. When $r = 1/\sqrt{2^{4/3}-1} \approx 0.811d$, the net force acting on each particle is zero. However, this force-balanced configuration has energy $-0.937/d$, which is higher than the energy $-1/d$ of a dipole plus an electron far away. Additionally, this classical trion has an unstable normal mode, where the hole moves toward one of the electrons along the $\mathbf{r}$ direction, making the classical trion a saddle point of the energy instead of a local minima.

Our above analysis of the classical three-body problem demonstrates that quantum mechanics is crucial for the formation of a trion bound state. As shown by numerical studies, the trion is the ground state of two electrons and one hole in the bilayer when $a_B/d > 0.065$ assuming equal electron and hole masses [45], where $a_B = (4\pi\epsilon\hbar^2/e^2m)$ is the Bohr radius (which vanishes in the classical limit $\hbar \to 0$ or $m \to \infty$). We can understand the trion's quantum origin heuristically. Start with the electron and the dipolar exciton separated by a large distance $r \gg d$, where they experience a static $1/r - 1/\sqrt{r^2+d^2} \propto d^2/r^3$ repulsion. On the other hand, the electron's in-plane electric field $\propto 1/r^2$ polarizes the exciton and lowers its energy through the second-order Stark effect by an amount $\delta E_s \propto -a_B^3/r^4$ to zeroth order in $d$. This quantum attraction dominates the classical electron-exciton repulsion over a range of distances below a crossover length $r_c \sim a_B^3/d^2$, supporting a trion bound state for sufficiently small $d$.

At finite charge density, an additional length scale appears: the average interparticle distance $a \equiv 1/\sqrt{\pi n}$, with $n = n_h$ for $n_e/n_h = 2$. With three length scales—the interparticle distance $a$, the layer distance $d$, and Bohr radius $a_B$, competition between intralayer repulsion, interlayer electron-hole attraction, and quantum kinetic energy yields a rich phase diagram for the electron-hole bilayer, which we explore below by a combination of analytical and numerical methods.

The Hamiltonian for the bilayer assuming equal electron and hole effective masses $m$ and $1/r$ Coulomb interactions is

$$H = \sum_{a=e,h}\sum_{s=\uparrow,\downarrow}\int \mathrm{d}^2\mathbf{r}\left[\psi_s^{a\dagger}(\mathbf{r})\left(\frac{-\nabla^2}{2}\right)\psi_s^a(\mathbf{r})\right] + \frac{1}{2}\int \mathrm{d}^2\mathbf{r}\int \mathrm{d}^2\mathbf{r}'\left[\sum_{a=e,h}\frac{n^a(\mathbf{r})n^a(\mathbf{r}')}{|\mathbf{r}-\mathbf{r}'|}\right] - \int \mathrm{d}^2\mathbf{r}\int \mathrm{d}^2\mathbf{r}'\left[\frac{n^e(\mathbf{r})n^h(\mathbf{r}')}{\sqrt{|\mathbf{r}-\mathbf{r}'|^2+d^2}}\right], \quad (1)$$

where $\psi^{e,h}(\mathbf{r})$ denotes the electron or hole operator, $n^a(\mathbf{r}) = \sum_s \psi_s^{a\dagger}(\mathbf{r})\psi_s^a(\mathbf{r})$ is the density operator, and $s$ denotes the spin. We have already divided all quantities by their appropriate atomic units, i.e., lengths by the Bohr radius $a_B = (4\pi\epsilon\hbar^2/me^2)$ (we use this definition throughout) and energies by the Hartree energy $E_h = (\hbar^2/ma_B^2)$. Unless stated otherwise, we assume for simplicity that the electron and hole masses are equal, noting that our main findings are qualitatively correct for a range of mass ratios.

*Classical regime.*—We first consider the classical limit defined by taking $a_B \to 0$ while keeping $d$ and $a$ fixed, or equivalently, $a/a_B \to \infty$ and $d/a_B \to \infty$ for a fixed $d/a$. In the classical limit, the phase diagram is characterized solely by the dimensionless ratio $d/a$. Both limits $d/a \gg 1$ and $d/a \ll 1$ can be understood analytically. When $d/a \gg 1$, the interlayer coupling is negligible and a triangular lattice Wigner crystal is formed independently in each layer. In the opposite regime $d/a \ll 1$, every hole pairs with an electron at the shortest possible distance $d$ to form a small out-of-plane dipole, leaving an equal number of excess electrons. These dipoles have a weak repulsion $1/r - 1/\sqrt{r^2+d^2} \propto d^2/r^3$ with the electrons, while electrons interact with each other through a strong Coulomb repulsion $1/r$. Therefore, the electrons arrange themselves essentially independently of the dipoles to form a triangular lattice Wigner crystal. Once the electrons crystallize, the dipoles crystallize in half of the voids between the electrons to minimize the residual repulsion. The result is a composite crystal of electrons and dipoles, where electrons occupy one sublattice of a honeycomb and dipoles occupy the other.

To determine the classical ground state as a function of the charge density, we minimized the classical electrostatic energy. To handle the Coulomb interaction's long-ranged tail, we used Ewald summation (see Supplemental Material [46]). For the experimentally relevant parameter range $a/d > 1$, we find two distinct composite crystals. For the low-density limit $a/d > 5.42$, the numerical results confirm our expectation of a honeycomb composite crystal. Interestingly, for $a/d < 5.42$ we find a "checkerboard" composite crystal consisting of two interpenetrating square lattices of electrons and dipoles. This is likely due to the increased electron-dipole repulsion at smaller $a/d$. We did not observe the formation of classical trions for any $a/d$, which is consistent with their instability. Once these two composite crystals were identified, we directly calculated their electrostatic energy as a function of $a/d$ and determined the phase transition point, which is shown in Fig. 1.

We now analyze the effect of quantum fluctuations around the classical composite crystals. At sufficiently small $a_B$, the leading quantum effect is the zero-point motion of charges in the classical ground state. The root-mean-square displacement of charges increases with $a_B$, and when it becomes comparable to the lattice constant $a$, quantum melting of the crystal occurs (Lindemann criterion) [55]. Since our composite crystals have three charges per unit cell, there are a total of six phonon modes, including both acoustic and optical branches. Notably, the

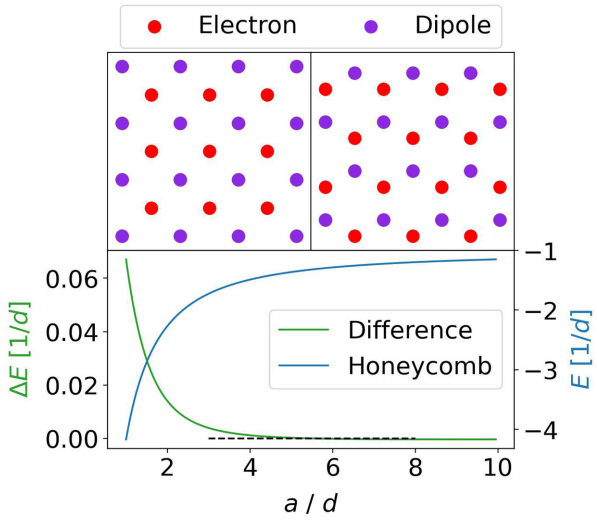


FIG. 1. The classical phase diagram of the electron-hole bilayer at $n_e/n_h = 2$ for $a/d > 1$. The top depicts the checkerboard composite crystal (left) and the honeycomb composite crystal (right). The bottom shows the energy and energy difference of the two composite crystals, with a dashed line indicating the phase transition.

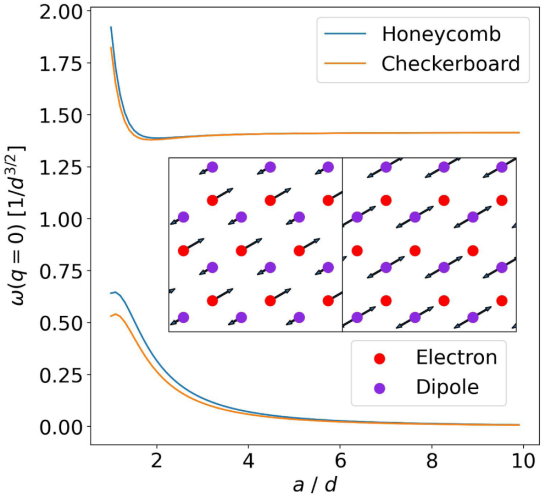


FIG. 2. Soft and hard optical phonon frequencies at the center of the Brillouin zone as function of $a/d$ for the classical composite crystals. The low-frequency branches correspond to the displacement of the dipole's center of mass relative to the electron, while the high-frequency branches are associated with oscillations in the dipole's internal structure.

optical phonons are associated with the relative vibration of charges within the unit cell, which is absent in the canonical electron Wigner crystal.

When the layer distance $d$ is small compared to the interparticle distance $a$, the electron-dipole repulsion in the composite crystal is much weaker than the electron-electron repulsion. Then we expect that the dipole's center of mass has the largest zero-point displacement, denoted as $\xi_d$. This is indeed confirmed by our direct calculation of the optical phonon frequencies at zero wave vector, which is shown in Fig. 2. Two types of optical phonons are present: the low-frequency one corresponds to the displacement of the dipole's center of mass relative to the electron, while the high-frequency one is associated with the internal structure of the dipole. At small $d/a$, the low-frequency optical phonon softens with $\omega_d \propto \sqrt{\partial_r^2 V(r)|_{r=a}/m} \propto \sqrt{d^2/ma^5}$ [where $V(r) \propto d^2/r^3$ is the electron-dipole potential], hence the zero-point displacement increases and is given by

$$\xi_d \sim \sqrt{\frac{\hbar}{m\omega_d}} \propto a\left(\frac{aa_B}{d^2}\right)^{1/4}. \tag{2}$$

In the classical limit $a_B/a \to 0$, $a_B/d \to 0$ with $a/d$ fixed, $\xi_d \ll a$ ensures the stability of the classical composite crystal against quantum fluctuation.

For small $d/a$, Eq. (2) implies that quantum melting of the dipole (= interlayer exciton) sublattice in the composite crystal occurs first when $a_B$ reaches the order of $d^2/a$. Meanwhile, the stronger electron-electron repulsion renders the electron lattice stable against quantum fluctuations until $a_B$ reaches the order of the interparticle distance $a$, as for the canonical Wigner crystal. This naturally raises the question of what the ground state is at intermediate $a_B$ between $d^2/a$ and $a$, where both quantum effects and electrostatic interactions play crucial roles.

*Dilute quantum regime.*—Of particular interest is the low-density limit defined by $a \to \infty$ while keeping $d$ and $a_B$ fixed, especially if $d$ and $a_B$ are of the same order. With $a \to \infty$, $a_B$ necessarily lies between $d^2/a$ and $a$, forcing partial melting of the composite crystal due to the zero-point motion of the excitons' center of mass.

The ground state in this low-density limit depends crucially on the ratio of the Bohr radius $a_B$ and layer distance $d$. For $d < d_c \approx 15.38a_B$ (assuming equal electron and hole masses), it is known from quantum Monte Carlo calculations that the lowest-energy state of two electrons and one hole is a trion bound state with the two electrons in a spin-singlet [45]. The spin-triplet trion is absent for $m_e = m_h$ and has a smaller binding energy when it is present for large mass ratio $m_e/m_h$ [45,56]. The trion's binding energy is on the order of $E_h$ at $d = 0$ and decreases as $d$ approaches the critical $d_c$ at which the trion unbinds. At a given $d < d_c$ and in the dilute limit $a \to \infty$, the hierarchy of energy scales is necessarily as follows: $E_{\text{trion}} \gg E_{\text{Coulomb}} \sim 1/a \gg E_{\text{kinetic}} \sim 1/a^2$.

The physically realistic parameters for the TMD bilayer $WSe_2/MoSe_2$ are electron effective mass $m_e(MoSe_2) = 0.8m_0$ ($m_0$ is the bare mass), hole effective mass $m_h(WSe_2) = 0.4m_0$, dielectric constant $\epsilon = 4.7\epsilon_0$, and interlayer spacing $d = 3$ nm [47–50]. With these numbers, the trion binding energy obtained from quantum Monte Carlo studies [45] is on the order of 15 K. Results from our Hartree-Fock calculations, which are

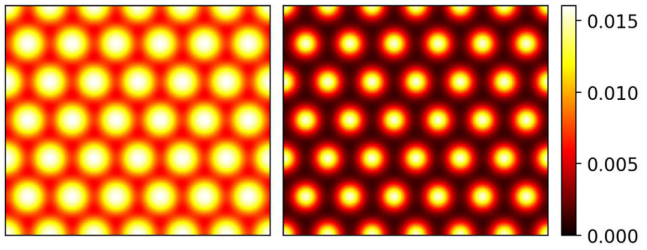


FIG. 3. The electron (hole) density is shown in the left (right) panel. The coloring scheme is consistent for both densities and is indicated by the color bar in units of $1/a_{B,h}^2$ for $a_{B,h} = (4\pi\epsilon\hbar^2/e^2 m_h)$. The calculation parameters are $m_e = 0.8m_0$, $m_h = 0.4m_0$, $d = 4.83a_{B,h}$, hole $r_s = 8$, $n_h = 36$, and equal electron spin populations.

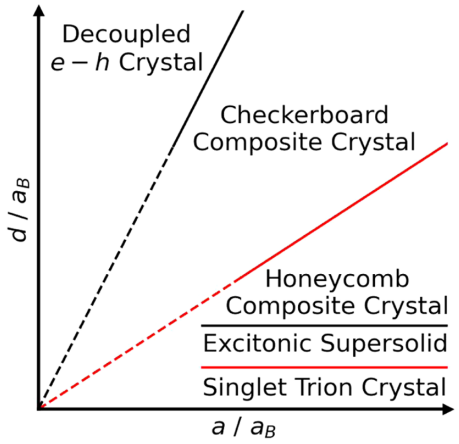


FIG. 4. Schematic phase diagram for the electron-hole bilayer at commensurate densities $n_e/n_h = 2$, with analytically known boundaries marked in red and limiting phases labeled.

shown in Fig. 3, confirm that the ground state with these parameters and a realistic trion density of $n_t = n_h = 1.29 \times 10^{12}$ cm$^{-2}$ (which corresponds to a trion density parameter $r_{s,\mathrm{trion}} = 40$ and hole density parameter $r_{s,\mathrm{hole}} = 8$) is an insulating quantum crystal (see Supplemental Material [46]).

We note that, although the Hartree-Fock method qualitatively captures many phases, including the trion Wigner crystal, it is generally biased toward symmetry-breaking phases and may not produce accurate phase boundaries. For our 2:1 bilayer, it is important to combine Hartree-Fock calculations with more advanced numerical methods to accurately determine the complete phase diagram. We have recently applied variational neural network wave functions to the balanced electron-hole bilayer and are planning a comprehensive study of the 2:1 bilayer with this technique in the future [57].

Notably, trions can crystallize at significantly higher densities than electrons or holes. Because of the trion's large binding energy ~15 K and small spatial extent ~$d$, in the trion Wigner crystal phase each trion behaves as a charge-$e$ fermion similar to an electron in an electron Wigner crystal. However, because the trion mass can be several times the electron mass, the trion's Bohr radius is several times smaller, so the same critical density parameter $r_s = 30$–$40$ corresponds to a much higher electron-hole density. For example, the $2e - 1h$ trion in $WSe_2/MoSe_2$ has total mass $2m_0$, allowing density parameter $r_s = 40$ to be reached at hole density $1.29 \times 10^{12}$ cm$^{-2}$. At these high densities, the effect of disorder and finite temperature is less severe, because all energy scales are larger. We also note that the possibility of trion crystallization in Van der Waals heterostructures has been considered recently [58,59].

Another distinctive feature of our trion Wigner crystal is that the electron layer has zero total spin and a large spin gap on the order of $E_h$ due to the trion binding energy, whereas the spins of localized holes interact with each other through a weak exchange interaction that vanishes in the low-density limit. Therefore, a small magnetic field can fully polarize the holes while leaving the spin-singlet electrons intact. This sharp contrast between the spin response of electron and hole layers is an indication of spin-singlet trion formation. As the density increases, the trion Wigner crystal could melt into a trion Fermi liquid before the trions dissociate. Such a metallic phase could be differentiated from the insulating trion Wigner crystal using transport measurements.

Finally, we discuss the regime $d > d_c$. Here, the trion is unstable at the three-particle level and unbinds into an electron and exciton. However, as shown earlier, the exciton sublattice in the composite crystal is necessarily unstable against quantum melting in the low-density limit. Consequently, we propose that, for $d > d_c$ and sufficiently low densities, the ground state is an exciton superfluid permeating through an electron crystal. This state is remarkable as it simultaneously exhibits crystallization and superfluidity. For this reason, we call it an electron-exciton supersolid, a quantum electron solid in which interstitial excitons Bose condense. Experimentally, this phase could be detected by Coulomb drag measurements. We also note that supersolid phases of excitons have been studied in density-balanced electron-hole bilayers [60–63].

We emphasize that our predicted phases are robust against perturbations to the model Hamiltonian in Eq. (1). For example, deviations from the $1/r$ potential at short distances are expected, which modifies the exciton and trion binding energies [64]. This shifts the phase boundaries (for example, between the electron-exciton supersolid and trion crystal), but does not change the many-body phases that we established in the dilute limit. We also note that coupling to phonons may lead to polaron formation [65], which would enhance the already high effective mass and make our phases even more robust.

*Conclusion.*—Our Letter introduces the electron-hole bilayer at commensurate 2:1 density ratio as a platform for realizing novel strong-coupling phases. We identify two

dimensionless ratios that govern the phase diagram: the ratio of the average interparticle spacing to the Bohr radius $a/a_B$ and the ratio of the interlayer spacing to the Bohr radius $d/a_B$. By a combination of theoretical analysis and numerical calculation, we find a number of ordered phases, shown schematically in Fig. 4. In the classical regime $a/a_B \gg 1$, $d/a_B \gg 1$, we identify three crystalline phases: decoupled crystals in each layer for small $a/d$, a checkerboard composite crystal composed of electrons and bound electron-hole dipoles for intermediate $a/d$, and a honeycomb composite crystal for large $a/d$. Focusing on the dilute regime $a \gg d, a_B$, as $d$ is decreased, we propose that large zero-point fluctuations of the excitons partially melt the composite crystal into an electron-exciton supersolid, where the unbound electrons remain crystalline, but the excitons condense into a superfluid. As $d$ is decreased further to the order of the Bohr radius $a_B$, we show that the second-order Stark effect mediates an effective attractive force between electrons and excitons. For sufficiently small $d$, this attraction binds excitons to electrons to form spin-singlet trions, which then subsequently crystallize into a trion crystal. Finally, we suggest that a combination of optical spectroscopy, transport, and Coulomb drag measurements may be used to experimentally observe our proposed phases.

Notably, the trion crystal is stable throughout the low charge density regime with a lattice constant varying continuously with the charge density $n = n_e - n_h$, provided that the electron-to-hole density ratio is maintained at the commensurate value $n_e/n_h = 2$. Thus, the trion crystal is charge compressible with $(\partial n/\partial \mu) \neq 0$, with $\mu$ the charge chemical potential, but has an energy gap to adding excitons, i.e., exciton incompressible. This should be contrasted with the excitonic insulator at charge neutrality $n = 0$, which is charge incompressible and exciton compressible. Remarkably, recent capacitance and optical experiments on $WSe_2/MoSe_2$ have shown that the charge and exciton compressibility can be measured independently by varying the top and bottom gate voltages concurrently with $\Delta V_B = \pm \Delta V_T$. Moreover, the formation of trion is accompanied by a reduction of spin susceptibility in the electron (majority carrier) layer, which can be detected by magnetic circular dichroism. Finally, it is noted that the binding energy of trions can be further increased by applying a magnetic field, which we leave to future study. We hope our theoretical work stimulates experimental study of TMD electron-hole bilayers at commensurate electron-hole density ratios.

*Note added.*—Very recently, evidence of spin-singlet trions have been observed in optical reflectance measurements and transport experiments in $WSe_2/MoSe_2$ [66,67].

We are grateful to Trithep Devakul and Aidan Reddy for helpful discussions. We thank Kin Fai Mak, Jie Shan, and Feng Wang for their interest and feedback. This work was supported by the Simons Investigator Award from the Simons Foundation. D. D. D. was supported by the Undergraduate Research Opportunities Program at MIT. The authors acknowledge the MIT SuperCloud and Lincoln Laboratory Supercomputing Center for providing high performance computing.

[1] F. Wu, T. Lovorn, E. Tutuc, and A. MacDonald, Phys. Rev. Lett. **121**, 026402 (2018).
[2] Y. Zhang, N. F. Yuan, and L. Fu, Phys. Rev. B **102**, 201115 (R) (2020).
[3] E. C. Regan, D. Wang, C. Jin, M. I. Bakti Utama, B. Gao, X. Wei, S. Zhao, W. Zhao, Z. Zhang, K. Yumigeta *et al.*, Nature (London) **579**, 359 (2020).
[4] Y. Tang, L. Li, T. Li, Y. Xu, S. Liu, K. Barmak, K. Watanabe, T. Taniguchi, A. H. MacDonald, J. Shan *et al.*, Nature (London) **579**, 353 (2020).
[5] T. Li, S. Jiang, L. Li, Y. Zhang, K. Kang, J. Zhu, K. Watanabe, T. Taniguchi, D. Chowdhury, L. Fu *et al.*, Nature (London) **597**, 350 (2021).
[6] H. Park, J. Zhu, X. Wang, Y. Wang, W. Holtzmann, T. Taniguchi, K. Watanabe, J. Yan, L. Fu, T. Cao *et al.*, Nat. Phys. **19**, 1286 (2023).
[7] Y. Xu, S. Liu, D. A. Rhodes, K. Watanabe, T. Taniguchi, J. Hone, V. Elser, K. F. Mak, and J. Shan, Nature (London) **587**, 214 (2020).
[8] Y. Zhou, J. Sung, E. Brutschea, I. Esterlis, Y. Wang, G. Scuri, R. J. Gelly, H. Heo, T. Taniguchi, K. Watanabe *et al.*, Nature (London) **595**, 48 (2021).
[9] C. Jin, Z. Tao, T. Li, Y. Xu, Y. Tang, J. Zhu, S. Liu, K. Watanabe, T. Taniguchi, J. C. Hone *et al.*, Nat. Mater. **20**, 940 (2021).
[10] H. Li, S. Li, E. C. Regan, D. Wang, W. Zhao, S. Kahn, K. Yumigeta, M. Blei, T. Taniguchi, K. Watanabe *et al.*, Nature (London) **597**, 650 (2021).
[11] X. Huang, T. Wang, S. Miao, C. Wang, Z. Li, Z. Lian, T. Taniguchi, K. Watanabe, S. Okamoto, D. Xiao *et al.*, Nat. Phys. **17**, 715 (2021).
[12] Y. Xu, K. Kang, K. Watanabe, T. Taniguchi, K. F. Mak, and J. Shan, Nat. Nanotechnol. **17**, 934 (2022).
[13] B. Padhi, R. Chitra, and P. W. Phillips, Phys. Rev. B **103**, 125146 (2021).
[14] C. Jin, Z. Tao, T. Li, Y. Xu, Y. Tang, J. Zhu, S. Liu, K. Watanabe, T. Taniguchi, J. C. Hone *et al.*, Nat. Mater. **20**, 940 (2021).
[15] Y. Zhang, H. Isobe, and L. Fu, arXiv:2005.04238.
[16] M. Davydova, Y. Zhang, and L. Fu, Phys. Rev. B **107**, 224420 (2023).
[17] L. Ciorciaro, T. Smolenski, I. Morera, N. Kiper, S. Hiestand, M. Kroner, Y. Zhang, K. Watanabe, T. Taniguchi, E. Demler *et al.*, Nature (London) **623**, 509 (2023).
[18] K. Lee, P. Sharma, O. Vafek, and H. J. Changlani, Phys. Rev. B **107** (2023).
[19] V. Crépel and L. Fu, Phys. Rev. B **107**, 235105 (2023).
[20] I. Morera, M. Kanász-Nagy, T. Smolenski, L. Ciorciaro, A. Imamoğlu, and E. Demler, Phys. Rev. Res. **5**, L022048 (2023).

[21] X. Wang, K. Yasuda, Y. Zhang, S. Liu, K. Watanabe, T. Taniguchi, J. Hone, L. Fu, and P. Jarillo-Herrero, Nat. Nanotechnol. **17**, 367 (2022).

[22] W. Zhao, B. Shen, Z. Tao, Z. Han, K. Kang, K. Watanabe, T. Taniguchi, K. F. Mak, and J. Shan, Nature (London) **616**, 61 (2023).

[23] A. Kumar, N. C. Hu, A. H. MacDonald, and A. C. Potter, Phys. Rev. B **106**, L041116 (2022).

[24] D. Guerci, J. Wang, J. Zang, J. Cano, J. H. Pixley, and A. Millis, Sci. Adv. **9**, eade7701 (2023).

[25] Y. Zhang and L. Fu, SciPost Phys. Core **6**, 038 (2023).

[26] Z. Tao, W. Zhao, B. Shen, P. Knüppel, K. Watanabe, T. Taniguchi, J. Shan, and K. F. Mak, arXiv:2307.12205.

[27] F. Wu, T. Lovorn, E. Tutuc, I. Martin, and A. MacDonald, Phys. Rev. Lett. **122**, 086402 (2019).

[28] W. Zhao, K. Kang, L. Li, C. Tschirhart, E. Redekop, K. Watanabe, T. Taniguchi, A. Young, J. Shan, and K. F. Mak, arXiv:2207.02312.

[29] T. Devakul, V. Crépel, Y. Zhang, and L. Fu, Nat. Commun. **12**, 6730 (2021).

[30] H. Li, U. Kumar, K. Sun, and S.-Z. Lin, Phys. Rev. Res. **3**, L032070 (2021).

[31] V. Crépel and L. Fu, Phys. Rev. B **107**, L201109 (2023).

[32] N. Morales-Durán, J. Wang, G. R. Schleder, M. Angeli, Z. Zhu, E. Kaxiras, C. Repellin, and J. Cano, Phys. Rev. Res. **5**, L032022 (2023).

[33] A. P. Reddy, F. F. Alsallom, Y. Zhang, T. Devakul, and L. Fu, Phys. Rev. B **108**, 085117 (2023).

[34] C. Wang, X.-W. Zhang, X. Liu, Y. He, X. Xu, Y. Ran, T. Cao, and D. Xiao, Phys. Rev. Lett. **132**, 036501 (2023).

[35] T. Li, S. Jiang, B. Shen, Y. Zhang, L. Li, Z. Tao, T. Devakul, K. Watanabe, T. Taniguchi, L. Fu *et al.*, Nature (London) **600**, 641 (2021).

[36] A. Kou, B. E. Feldman, A. J. Levin, B. I. Halperin, K. Watanabe, T. Taniguchi, and A. Yacoby, Science **345**, 55 (2014).

[37] J. Cai, E. Anderson, C. Wang, X. Zhang, X. Liu, W. Holtzmann, Y. Zhang, F. Fan, T. Taniguchi, K. Watanabe *et al.*, Nature (London) **622**, 63 (2023).

[38] Y. Zeng, Z. Xia, K. Kang, J. Zhu, P. Knüppel, C. Vaswani, K. Watanabe, T. Taniguchi, K. F. Mak, and J. Shan, arXiv:2305.00973.

[39] Y. Zeng and A. H. MacDonald, Phys. Rev. B **102**, 085154 (2020).

[40] L. Ma, P. X. Nguyen, Z. Wang, Y. Zeng, K. Watanabe, T. Taniguchi, A. H. MacDonald, K. F. Mak, and J. Shan, Nature (London) **598**, 585 (2021).

[41] R. Qi, A. Y. Joe, Z. Zhang, Y. Zeng, T. Zheng, Q. Feng, E. Regan, J. Xie, Z. Lu, T. Taniguchi *et al.*, arXiv:2306.13265.

[42] L. Ma, P. X. Nguyen, Z. Wang, Y. Zeng, K. Watanabe, T. Taniguchi, A. H. MacDonald, K. F. Mak, and J. Shan, Nature (London) **598**, 585 (2021).

[43] Y. Koo, H. Lee, T. Ivanova, A. Kefayati, V. Perebeinos, E. Khestanova, V. Kravtsov, and K.-D. Park, Light **12**, 59 (2023).

[44] J. Pei, J. Yang, R. Xu, Y.-H. Zeng, Y. W. Myint, S. Zhang, J.-C. Zheng, Q. Qin, X. Wang, W. Jiang *et al.*, Small **11**, 6384 (2015).

[45] O. Witham, R. J. Hunt, and N. D. Drummond, Phys. Rev. B **97**, 075424 (2018).

[46] See Supplemental Material at http://link.aps.org/supplemental/10.1103/PhysRevLett.132.196202, for additional information on and detailed discussion of the supporting numerical work, which includes Refs. [47–54].

[47] S. Larentis, H. C. Movva, B. Fallahazad, K. Kim, A. Behroozi, T. Taniguchi, K. Watanabe, S. K. Banerjee, and E. Tutuc, Phys. Rev. B **97**, 201407 (2018).

[48] P.-C. Yeh, W. Jin, N. Zaki, D. Zhang, J. T. Liou, J. T. Sadowski, A. Al-Mahboob, J. I. Dadap, I. P. Herman, P. Sutter *et al.*, Phys. Rev. B **91**, 041407 (2015).

[49] B. Fallahazad, H. C. P. Movva, K. Kim, S. Larentis, T. Taniguchi, K. Watanabe, S. K. Banerjee, and E. Tutuc, Phys. Rev. Lett. **116**, 086601 (2016).

[50] A. Laturia, M. L. Van de Put, and W. G. Vandenberghe, npj 2D Mater. Appl. **2**, 6 (2018).

[51] R. E. Johnson and S. Ranganathan, Phys. Rev. E **63**, 056703 (2001).

[52] T. A. Arias, M. C. Payne, and J. D. Joannopoulos, Phys. Rev. Lett. **69**, 1077 (1992).

[53] R. Sundararaman, K. Letchworth-Weaver, K. A. Schwarz, D. Gunceler, Y. Ozhabes, and T. Arias, SoftwareX **6**, 278 (2017).

[54] I. Mayer, Int. J. Quantum Chem. **90**, 63 (2002).

[55] G. Goldoni and F. M. Peeters, Phys. Rev. B **53**, 4591 (1996).

[56] E. Mostaani, M. Szyniszewski, C. H. Price, R. Maezono, M. Danovich, R. J. Hunt, N. D. Drummond, and V. I. Fal'ko, Phys. Rev. B **96**, 075431 (2017).

[57] D. Luo, D. D. Dai, and L. Fu, arXiv:2311.02143.

[58] I. V. Bondarev, O. L. Berman, R. Y. Kezerashvili, and Y. E. Lozovik, Commun. Phys. **4**, 134 (2021).

[59] I. V. Bondarev and Y. E. Lozovik, Commun. Phys. **5**, 315 (2022).

[60] S. Conti, A. Perali, A. R. Hamilton, M. V. Milošević, F. M. Peeters, and D. Neilson, Phys. Rev. Lett. **130**, 057001 (2023).

[61] V. W. Scarola and S. Das Sarma, Phys. Rev. Lett. **95**, 033003 (2005).

[62] V. W. Scarola, E. Demler, and S. Das Sarma, Phys. Rev. A **73**, 051601 (2006).

[63] Y. N. Joglekar, A. V. Balatsky, and S. Das Sarma, Phys. Rev. B **74**, 233302 (2006).

[64] M. A. Semina, Phys. Solid State **61**, 2218 (2019).

[65] Y. Mao, X. Ma, D. Wu, C. Lin, H. Shan, X. Wu, J. Zhao, A. Zhao, and B. Wang, Nano Lett. **20**, 8067 (2020).

[66] R. Qi, Q. Li, Z. Zhang, S. Chen, J. Xie, Y. Ou, Z. Cui, D. D. Dai, A. Y. Joe, T. Taniguchi *et al.*, arXiv:2312.03251.

[67] P. X. Nguyen, R. Chaturvedi, L. Ma, P. Knuppel, K. Watanabe, T. Taniguchi, K. F. Mak, and J. Shan, arXiv:2312.12571.